Heit, B., Yuan, X., Bianchi, M., Kind, R., Gossler, J. (2010): Study of the lithospheric and upper-mantle discontinuities beneath eastern Asia by SS precursors. - Geophysical Journal International, 183, 1, pp. 252—266.

DOI: http://doi.org/10.1111/j.1365-246X.2010.04714.x

Geophysical Journal International

Geophys. J. Int. (2010) **183,** 252–266 doi: 10.1111/j.1365-246X.2010.04714.x

Study of the lithospheric and upper-mantle discontinuities beneath eastern Asia by *SS* precursors

Benjamin Heit,[1] Xiaohui Yuan,[1] Marcelo Bianchi,[2] Rainer Kind[1,3] and Jürgen Gossler[4]

[1] *Deutsches GeoForschungsZentrum GFZ, Telegrafenberg,* 14473 *Potsdam, Germany. E-mail: heit@gfz-potsdam.de*
[2] *Schlumberger, Stavanger, Norway*
[3] *Freie Universität Berlin, Germany*
[4] *AWI Bremerhaven, Am Alten Hafen* 26, 27568 *Bremerhaven, Germany*

Accepted 2010 June 23. Received 2010 June 21; in original form 2010 February 19

SUMMARY

We analyse broad-band *SS* waveform data recorded by several networks in Europe with sources mainly in the west Pacific to study the underside reflections of teleseismic *SS* waves in the lithosphere and the upper mantle beneath eastern Asia and the NW Pacific ocean. *SS* bounce points sample a corridor from the Aleutian, Kamchatka and Japan subduction zones through the North China Craton and Central Asian Orogenic Belt to the Tibetan plateau. The corridor passes through different tectonic units such as subduction zones, an old continental shield, a fold belt and a high plateau. We investigate the seismic structure of the lithosphere and the mantle transition zone beneath the different geotectonic units along the profile and infer the correlation of geodynamic processes at different depths. We explore the short period frequency content in the *SS* waveform data and use moveout correction and common midpoint stack to acquire profiles with high lateral and depth resolution from the crust to the mantle transition zone. Clear *SS* precursors of the 410 and 660 km discontinuities show the effects of the interaction between the subducted oceanic lithosphere and the mantle transition zone beneath the NW Pacific subduction zones. A low-velocity layer has also been detected beneath the 410 km discontinuity and can be traced along the entire profile. Due to the improved resolution acquired by the method presented here we have been able to study the shallower structures such as the Moho and the lithosphere–asthenosphere boundary by *SS* precursors. The continental Moho can be clearly seen along this corridor. The depth variation agrees well with earlier receiver function results. We also see negative reflectors along the profile at varying depths, which can be interpreted as the lithosphere–asthenosphere boundary.

Key words: Time series analysis; Body waves; Wave scattering and diffraction.

GJI Seismology

1 INTRODUCTION

The Earth's mantle is divided into layers according to seismic velocity variations detected by the propagation of body waves. These layers or zones are mainly defined by the presence of certain mineral stable phases. Mantle minerals such as olivine, pyroxene and garnet (e.g. Ringwood 1969; Helffrich 2000) are subject to changes as pressure and temperature increases. When this occurs, phase transformations take place that are responsible for seismic discontinuities. Unlike the crust–mantle boundary (Moho), which is widely accepted as compositional change, the lithosphere–asthenosphere boundary (LAB) was originally defined with regards to rheology, with the lithosphere behaving essentially as elastic solid and the asthenosphere deforming as a viscous fluid (Barrell 1914). Since then, additional definitions of the term lithosphere have been introduced such as thermal, seismic or chemical lithosphere (Anderson 1995; Eaton *et al.* 2009). Observations from the high seismic velocity mantle lid are interpreted as being indicative of the seismic lithosphere. The major mineral component in the upper mantle is the alpha-phase olivine that remains stable down to ∼410 km depth and then undergoes a number of phase changes. The most prominent phase transformations are the ones responsible for the mantle transition zone (MTZ) that separates the upper and lower mantle. The MTZ is globally located between 410 and 660 km depth and is characterized by abrupt increases in seismic velocities and densities reflecting the changes in olivine that undergoes phase transformations from low- to high-pressure forms (recently reviewed by Frost 2008). Named as the global average depth, the 410 km discontinuity (the 410) marks the transition from olivine to wadsleyite, and the 660 km discontinuity (the 660) marks the transition from ringwoodite to perovskite + magnesiowustite. Experimental studies have shown that both reactions are sensitive to temperature and have Clapeyron slopes that are opposite in sign (Bina & Helffrich 1994). In the absence of other effects, a lateral increase in temperature at

the level of the transition zone should be reflected in a deepening of the 410 km discontinuity and a shallowing of the 660 km discontinuity (and vice versa). In the presence of a disturbing feature as an oceanic slab, the colder temperatures should shift the 410 upwards and the 660 downwards (e.g. Tonegawa *et al.* 2005), whereas hot-mantle plumes should shift both the 410 and the 660 closer together.

The temperature in the MTZ, which strongly influences the mechanical strength of the mantle materials, can be derived from the thickness of the transition zone (Helffrich 2000). Inside the MTZ the transition from wadsleyite to ringwoodite, the 520 km discontinuity (named the 520), is probably a gradient phase change (e.g. Katsura & Ito 1989) and may occur at varying depth levels. Therefore the 520 is not observed globally. In some regions, phase transformations of minor mantle constituents, such as garnet, become significant and cause complication in the MTZ structures (Vacher *et al.* 1998).

Seismic discontinuities in the crust and upper mantle may generate reflections and mode conversions of seismic body waves and therefore can be visualized by looking at reflected and converted seismic waves. Receiver function and *SS* precursor analysis are two well-known methods. Receiver functions contain *P*-to-*S* converted phases below the stations. The method is applicable mostly on continents or islands where seismic stations can be deployed. *SS* precursors are underside reflected *SS* waves off a given reflector as the mantle discontinuities below *SS* bounce points, located in remote areas halfway between earthquakes and receivers and therefore can be used to globally map the mantle discontinuities (Fig. 1). Among other authors, Shearer (1991) has shown, for example, the potentials to investigate the mantle discontinuities by globally stacking *SS* precursor data.

The 410 and 660 km discontinuities used to be the main objects of previous studies using *SS* precursors, because they are the most significant phases in the *SS* data (e.g. Shearer 1991; Shearer & Masters 1992; Petersen *et al.* 1993; Shearer 1993; Gossler & Kind 1996; Flanagan & Shearer 1998; Gu *et al.* 1998; Gu & Dziewonski 2002; Chambers *et al.* 2005a, b; Deuss 2009). The 520 km discontinuity has also been identified by a number of studies (e.g. Shearer 1990; Gossler & Kind 1996; Shearer 1996; Flanagan & Shearer 1998; Deuss & Woodhouse 2001) but its global existence is still under discussion. In addition, there are observations of other discontinuities at various depths as is the case of the Lehmann discontinuity at *ca*. 220 km depth (Gu *et al.* 2001; Deuss & Woodhouse 2002) and the 900 km discontinuity (Petersen *et al.* 1993).

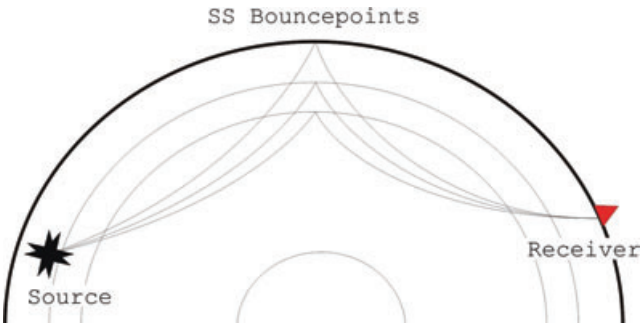

Figure 1. Schematic cartoon showing the *SS* bounce points sampling remote areas located halfway between earthquakes and receivers to map the mantle discontinuities.

Seismic methods in local or regional scale are basically very useful in continental areas with high levels of seismic activity in correlation with well-designed networks and dense station distribution to obtain relatively reliable images of the upper mantle. The use of *SS* precursors has an overall advantage over other methods as it enables us to sample relatively large areas where no stations are deployed. In this way, it is possible to analyse a region that spans over 100° in Asia, which gives us the opportunity to integrate different geodynamic areas. This global view can help us to improve the quality and resolution of upper-mantle discontinuities and understand their distribution in correlation with different tectonic regions.

Most of the previous studies used long-period *SS* waveform data and have restricted the discussion to the long-wavelength topography of the MTZ discontinuities and its implication for lateral variations in the MTZ temperatures. The results show general agreement in a global scale but some discrepancies remain in the details while analysing the regional aspects of them. Some authors (e.g. Gossler & Kind 1996; Gu & Dziewonski 2002; Li *et al.* 2003) claimed that there is a correlation between the MTZ thickness (or temperature) and the distribution of major continental and oceanic plates, suggesting that the ocean–continent differences may extend into the MTZ. However, this correlation has not been evident in other studies (e.g. Shearer 1993; Flanagan & Shearer 1998). Shearer (1991) and Shearer & Masters (1992) observed a thickening of the MTZ in the northwest Pacific subduction, while Petersen *et al.* (1993) found there a thinning of the MTZ . The observation of a large-scale (over 1000 km) thickening of the MTZ (Shearer, 1991; Shearer & Masters 1992) beneath NE China was interpreted as the effect of stagnation of the Pacific slab over 1000 km. This idea is partly supported by some receiver function studies (e.g. Vinnik *et al.* 1996), whereas other studies (Li *et al.* 2000; Li & Yuan 2003) with much higher resolution have detected a transition zone thickening only in the vicinity of the slab.

The reason for the discrepancies in these observations could be related to the different size of the bounce points regions used to perform the stacking technique or trace summation (e.g. 30° in Gossler & Kind (1996) and 10° radius in Gu & Dziewonski (2002) and Flanagan & Shearer (1998)). Furthermore, Gu & Dziewonski (2002) averaged their *SS* precursor data to produce a $30^\circ \times 30^\circ$ cap size as well and came to a similar conclusion as Gossler & Kind (1996). A new model presented by Chambers *et al.* (2005a,b) shows that the long-wavelength anomaly pattern in the mantle is a temperature effect, while on the other hand, at shorter wavelengths the influence of chemical heterogeneities becomes more visible in seismic velocity anomalies and mantle discontinuity topography. Shearer (2000) suggested that discrepancies in the observations might be related either to different processing methods or the wrong correction applied to crustal and upper-mantle structures.

However the spatial resolution is so far low (more than 1000 km) due to long wavelength of *SS* waves and the stacking method used (e.g. Neele *et al.* 1997). A low-pass filter of >20 s is normally applied to enhance the signal-to-noise (S/N) ratio. Furthermore, *SS* precursor signals are rarely detected in individual traces. A slowness stack of the deconvolved *SS* seismograms with bounce points located within big caps ($30^\circ \times 30^\circ$ in Gossler & Kind 1996; $10^\circ \times 10^\circ$ in Flanagan & Shearer 1998 and Gu & Dziewonski 2002) is usually used to identify the precursors to the *SS* phases. Due to low resolution, the method appears to be invalid to detect discontinuities in the shallow mantle, such as the Moho and the LAB.

The resolution of *SS* precursors may be increased by looking at individual traces. An approach analogue to the common midpoint

(CMP) stacking used in reflection seismology can be applied to stack the *SS* data. The technique has already shown its big success when it was introduced into the receiver function processing (Dueker & Sheehan 1997; Yuan *et al.* 1997). The arrival time of the *SS* precursor with reference to the *SS* arrival is a function of the epicentral distance (moveout). Prior to stacking a moveout correction should be applied to correct for the difference in the epicentral distance. In this work, we create a CMP profile of *SS* precursor data in east Asia and NW Pacific with seismic permanent stations located in Europe. We preserve the high-frequency content of the *SS* waveform data and improve the lateral and depth resolution for the upper-mantle discontinuities and hence create new possibilities to study the shallower structures such as the LAB and the continental Moho by using *SS* precursors.

2 THE *SS* PRECURSOR TRANSECT

Fig. 2(a) shows a map of *SS* bounce points for the European seismic stations and globally distributed earthquakes within epicentral distances of 100°–180°. Most of the events are located in west Pacific that goes from the Fiji-Tonga to the Indonesian subduction zone.

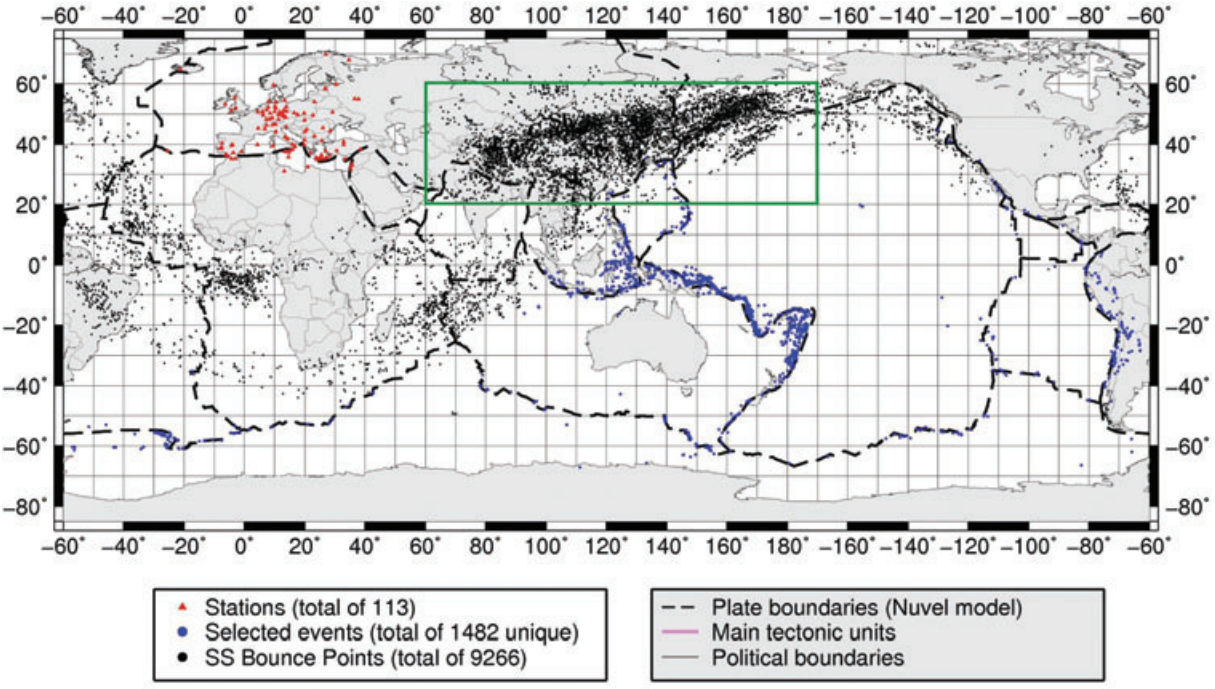

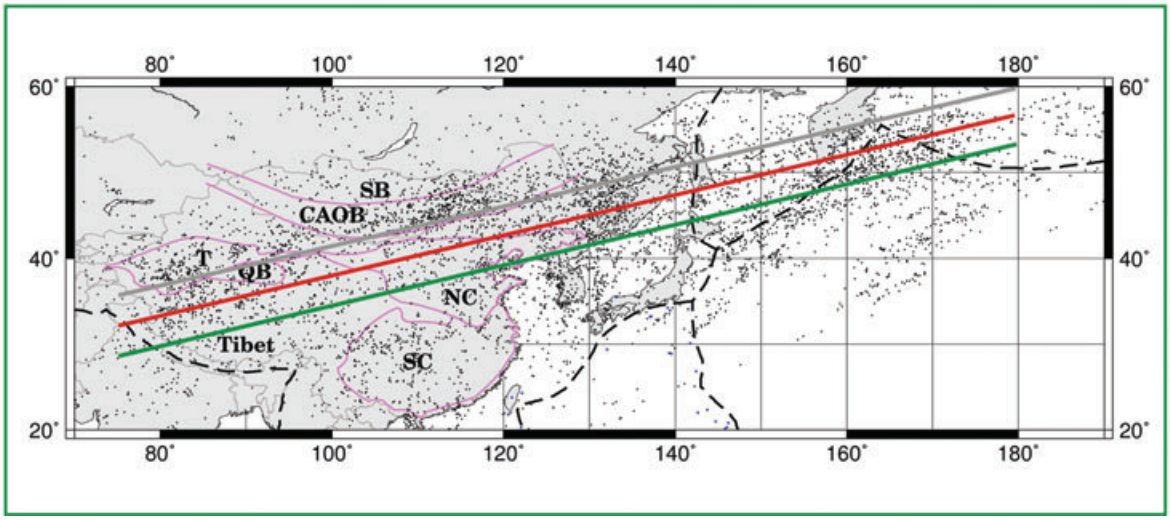

Figure 2. Top panel: map of earthquakes and stations from IRIS and the GEOFON, GRSN and GRF networks used in this study. The earthquakes with epicentral distances between 100° and 180° are displayed in blue colour and are used to search for *SS* precursors. The black dots represent the bounce points. The stations (113 in total) are displayed in red colour. The study area is marked in green. Bottom panel: the grey, red and green lines represent the position of the profiles performed in this study. The region includes the bounce points located along the corridor from the Aleutians, Kamtchatka, Sino-Korean craton and the Tibetan plateau. SB: Siberian Block; CAOB: Central Asian Orogenic Belt; NC: North China Craton; SC: South China Craton; QB: Qaidam Basin; T: Tarim Basin.

The *SS* bounce points are concentrated along a corridor from NW Pacific Ocean to the northern part of the Tibetan plateau. The distribution of the finally selected *SS* bounce points facilitate the analysis of the three profiles from 75°E to 180°E between 25°N and 60°N (Fig. 2b). These profiles are designed to sample the lithosphere and upper mantle beneath different tectonic units from the western Tibetan plateau, throughout a series of old continental blocks to the Pacific subduction zone on the east. The study area is very complex from the geological and tectonical point of view as it includes the presence of subducting oceanic plates on the east (i.e. the Pacific and Philippine Sea plates), old cratonic areas in the centre [e.g. North China Craton (NC)] and the elevated Tibetan plateau with many sutures that reflect the collision of two different continental units on the west. This area has been the subject of many scientific studies involving, for example, tomography (e.g. Bijwaard *et al.* 1998; Zhao 2004; Huang & Zhao 2006; Kustowski *et al.* 2008) and receiver function (e.g. Li *et al.* 2000; Li & Yuan 2003, Nabelek *et al.* 2009) among other geophysical methods but unfortunately, clarifying images from the interaction between the MTZ discontinuities and the different tectonics units have not yet been presented. In the lithosphere and the upper mantle the situation is similar as many questions related to the distribution and topography of the discontinuities remain open.

There are although indications that suggest some correlations between the upper mantle and the structures observed in the crust as they might be indicating zones with seismic velocities relative to the presence of some major faults in the crust. Whether the subducted slab is affecting the topography of the MTZ in this region is still under discussion. The collision between India and Asia started 50 Ma and has been since then controlling the crustal and upper-mantle processes that accompanied the tectonic evolution and uplift of the crustal blocks. The different blocks in this area are represented by a very old collage of microblocks that have been interacting since the Archean (e.g. Kusky *et al.* 2007). Among the most important in size, in this region, are the Siberian Block (SB), the Tarim Block (TB), the Qaidam Basin (QB), the NC, the Central Asian Orogenic Belt (CAOB) and the South China Craton (SC) (see Fig. 2b). The CAOB on the north represents a collage of microplates, ophiolitic complexes, accretionary wedges and magmatic arcs (e.g. Kröner *et al.* 2007, 2008; Windley *et al.* 2007). The suture zones from the CAOB represent palaeosubduction boundaries that penetrate the entire crust and reach the upper portions of the mantle (e.g. Kröner *et al.* 2007).

Surface wave studies revealed an eastward thinning of the lithosphere beneath China with a lithospheric thickness that goes from ∼200 km beneath Tibet and the Tarim Basin to less than 100 km beneath east China (Huang *et al.* 2003; Priestley & McKenzie 2006). This result is partly confirmed by the *S* receiver function studies (Kumar *et al.* 2006; Sodoudi *et al.* 2006; Chen *et al.* 2008) where it is possible to realize that the structure of the lithosphere and MTZ becomes more complicated in the proximity to subduction zones. Some tomographic studies suggest the penetration of the slab into the lower mantle as well as slab stagnation within the MTZ (e.g. Van Der Hilst *et al.* 1991; Fukao *et al.* 1992; Bijwaard *et al.* 1998; Van Der Voo *et al.* 1999).

Shearer & Masters (1992) and Shearer (1991) found a large-scale deepening of the 660 in the northwest Pacific region which is consistent with the slab deflection, while Gu & Dziewonski (2002) suggested a less pronounced variation of the 660 in the west Pacific than previous *SS* studies. Receiver function studies (Li *et al.* 2000; Li & Yuan 2003) found no deepening of the 660 to the northwest of the Pacific subduction zone and concluded that deepening of the 660 likely occurs locally where the plate penetrates the MTZ.

3 METHODOLOGY

As sketched in Fig. 1 the underside reflected *SS* waves (named *SdS*, where *d* represents the depth of the reflector) off discontinuities in the crust and mantle propagate along a similar path from the source to the receiver as that of the *SS* wave. Due to shorter paths the *SdS* waves arrive earlier than the reference phase *SS* does and therefore appear as precursors to the *SS* phase in the seismogram. The depth of the reflector can be estimated by measuring the time difference between the *SdS* and *SS* phases. This time difference can be estimated by

$$t_{SdS} = 2\int_0^d \mathrm{d}z\sqrt{v_S^{-2}(z) - p^2},$$

where d is depth of the reflector, p is *SS* slowness, $v_S(z)$ is shear wave velocity as a function of depth and $\sqrt{v_S^{-2}(z) - p^2}$ is the vertical slowness. The equation is based on a plane wave assumption, which is valid as long as the paths of the *SdS* and *SS* phases are close

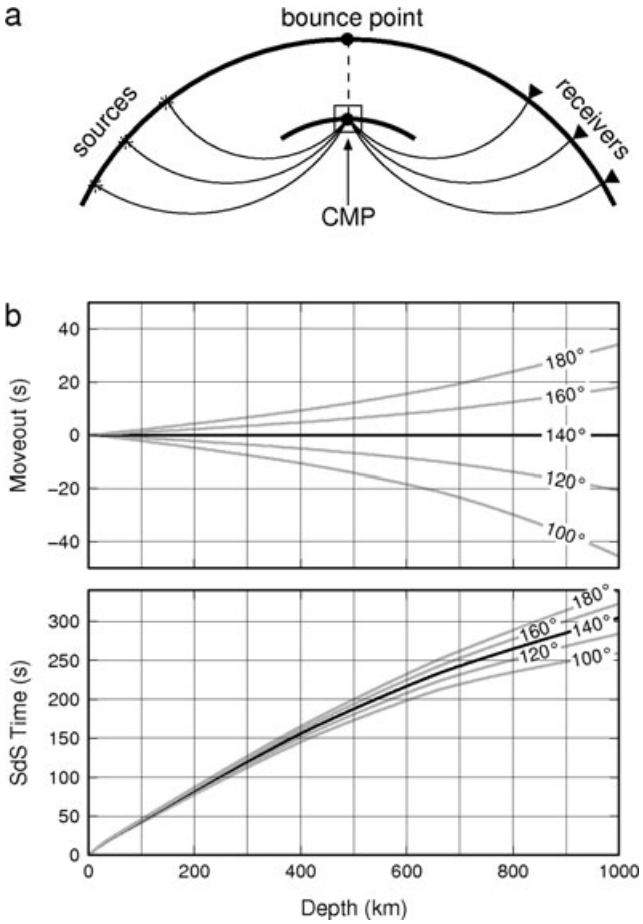

Figure 3. (a) Sketch showing the common midpoints of *SdS* paths with different epicentral distances. (b) Top panel: moveout effect in seconds of the *SdS* according to the bouncing depths in kilometres. Bottom panel: *SdS* arrival times prior to the *SS* phase for different reflection depths (horizontal axis) and different epicentral distances (labelled on curves). The reference distance of 140° used in this paper, as seen in this graphic, is the middle of the epicentral distance between 100° and 180° enables us to get a good recovery of the signals from the upper 1000 km.

to each other. This is true for reflectors in the upper mantle. The deviation of the plane wave assumption from a spherical model at a distance of 140° is about 0.5 s (1.5 km in terms of reflection depth) for the *S*410*S* and about 1.8 s (5 km) for the *S*660*S*. The arrival time of the *SS* precursor with reference to the *SS* arrival is a function of the epicentral distance (Fig. 3a). The distance dependence of the arrival time is called moveout. The moveout increases as the depth of the reflector increases. For a range of epicentral distances of 100°–180° the moveout is ∼20 s for the *S*410*S* and ∼40 s for the *S*660*S* (Fig. 3b). Therefore, the moveout should be corrected before stacking *SS* waveform data.

There are different ways of performing a moveout correction. In Fig. 4 we demonstrate the moveout method applied on synthetic seismograms generated by the reflectivity method (Kind 1978). The chosen model is based on the IASP91 model, but contains a simplified one-layer crust, a low-velocity layer in the upper mantle representing the asthenosphere, with its upper boundary located at 120 km (labelled LAB) and a velocity increase at 210 km (i.e. the Lehmann discontinuity, labelled 210) (Fig. 4a).

In our processing, we used a dominant wave period of ∼11 s, which represents well the *SS* waveform data presented in this paper and is shorter than those used in the previous long-period studies as in the case of Shearer (1991) where the dominant wave period is 25 s. In the original *SH* seismograms aligned by the *SS* arrivals (Fig. 4b), we see clearly the precursors of the mantle discontinuities (the LAB, 210, 410 and 660). The Moho appears at ∼20 s, close to the *SS* phase, and therefore may be possibly covered by the sidelobe of the strong *SS* waveforms but as we will see later we have been able to obtain signals from the continental Moho along our profiles.

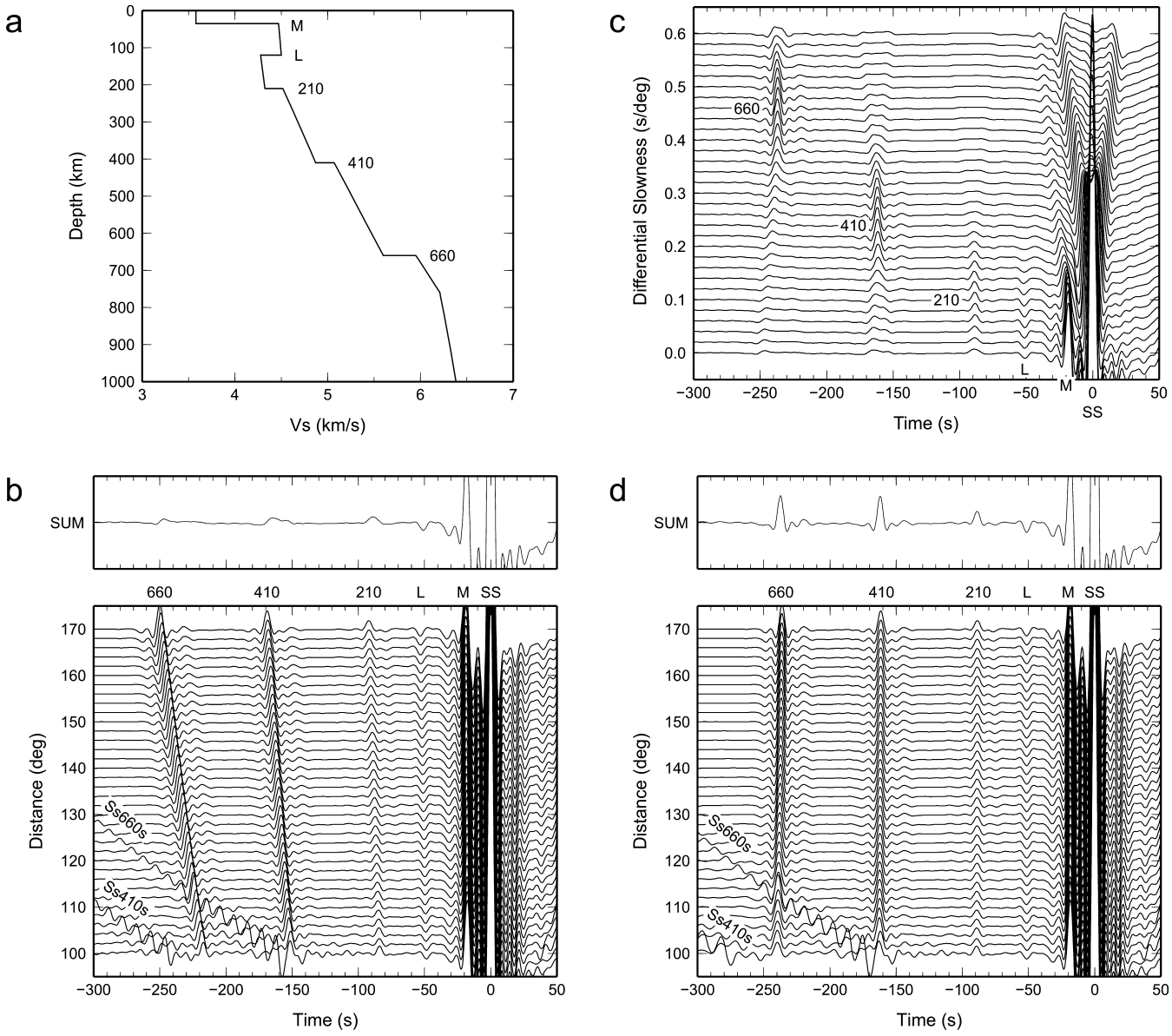

Figure 4. (a) V_s model used for calculation of synthetic seismograms. (b) Synthetic *SS* wave seismograms generated by the reflectivity method (Kind 1978). *SH* seismograms are calculated at epicentral distances of 100°–170° for a vertical dip-slip source located at the surface. The traces are deconvolved and aligned by the *SS* arrivals. Simple summation (the top trace SUM) does not reveal the discontinuity phases due to the moveout effect. (c) Slant stack of *SS* data with a reference distance of 140°. Each discontinuity phase can be clearly seen at its corresponding differential slowness. (d) *SS* data after moveout correction with a reference distance of 140°. The traces are vertically aligned and the discontinuities are well recognized in the summation trace.

However, the discontinuities cannot be simply identified in the summation trace (Fig. 4b) due to the moveout effect. To solve this problem it is possible to apply the slant stack to correct for the moveout. The slant stack technique can enhance the precursor phases at the corresponding differential slowness (Fig. 4c). The technique is sometimes also called slowness stack or delay-and-sum and has often been used in previous studies (e.g. Gossler & Kind 1996). This method may be used to identify reflected phases at right slowness and to check if the traces have been effectively stacked. However it also neglects the information of lateral structural variations contained in the individual *SS* traces. Sometimes due to lateral heterogeneities or the use of an unfavourable velocity model, the stacking is not able to enhance the discontinuities.

A dynamic moveout correction can be applied to the individual *SS* traces. Every individual trace is moveout corrected sample by sample (Fig. 4d). As a result, all the discontinuity phases are vertically aligned and clearly shown in the summation trace. The CMP stack technique allows us to sort and stack individual *SS* data by geographical locations of the bounce points (Fig. 3) and makes it possible to create high-resolution *SS* precursor profiles. Reference distance used in this paper is 140°, which is in the middle of the epicentral distance range between 100° and 180°.

4 DATA PROCESSING AND CMP STACKING

We analysed broad-band *SS* waveform data obtained from permanent stations located in Europe from a number of seismological networks. Seismograms were requested from GEOFON and IRIS data centres. The GRF array has been operating for more than 30 years. The GRSN network has more than 20 stations, most of which have been operated for more than 10 yr. The GEOFON stations are mostly distributed in Europe with an operation time of 5–10 yr. Many other national or international networks, which contribute continuous data to the IRIS, have also operated for some 5–10 yr. These stations recorded numerous high-quality earthquake waveform data that are well suited for stacking of *SS* precursor data.

The processing of the *SS* precursors includes basically coordinate rotation, data selection, filtering and deconvolution. The N and E components are rotated into the radial (R) and transversal (T) components. The coordinate rotation is performed using the event-station. Seismograms are selected by a criterion of good S/N ratio of *SS* phase. TT components are first aligned by the *SS* arrival. The S/N ratio is estimated between windows 30 s after and 400 s before the *SS* arrival. A two-pole bandpass filter (45 s–6 s) was applied for calculating the S/N ratio. Bad traces with S/N ratio less than 1.45 are removed. A window of 85 s of *SS* waveforms on the component is deconvolved from the same trace (Fig. 5). Moveout correction for a reference of 140° (*SS* slowness of 11.726 s deg^{-1}) is applied to each individual trace. The resulted traces are grouped by bins or boxes of locations of common-midpoints (bounce points) and are stacked to enhance signals of coherent.

In Fig. 6, all processed *SS* waveforms contained in the green area from Fig. 2 are stacked in a similar way as in the case of the synthetic *SS* stacks in Fig. 4. All bounce points are distributed along the whole transect over a distance of 100°. The positive amplitudes are coded blue and the negative red. The slant stack section (Fig. 6a) is dominated by the *S*410*S* and *S*660*S* phases, which arrive at 161 and 236 s before the *SS* arrival (at 0 s), respectively, 2–3 s earlier than expected by the IASP91 model (159 and 233 s, respectively, estimated by a plane wave assumption for a reference distance of 140°). Compared to the IASP91 model the simultaneous increase (2 s) in the *S*410*S* and *S*660*S* times may indicate a reduced average *S*-wave velocity in the upper mantle, while the slight increase (1 s) in the time difference between *S*410*S* and *S*660*S* may suggest a slightly thickened MTZ. There is evidence for the 520 phase, but it is very weak. At shallower depths (times closer to the *SS* arrival) a band of positive amplitudes spread in the time window of 50–100 s, corresponding to a depth range of 100–250 km (see Fig. 3). The band may be a mixture of noise and some reflectors at varying depths along the profile. The Moho (<25 s) is overwhelmed within the strong *SS* sidelobes. Fig. 6(b) is a binning section stacked over the entire distance range. The *S*410*S* and *S*660*S* phases show significant moveout and are therefore hardly recognized in the summation

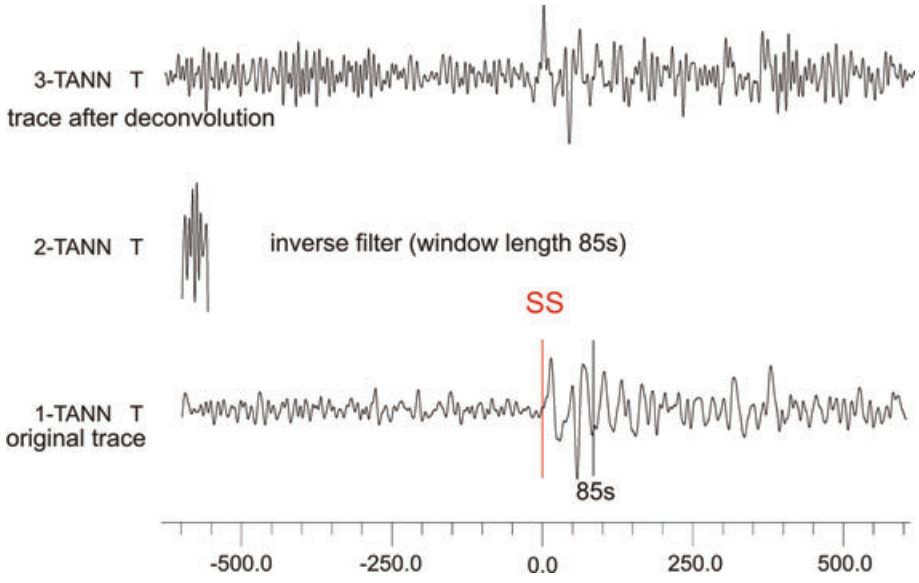

Figure 5. Example for station TANN (Tannbergstahl, Germany) of the procedure after searching for traces with good signal-to-noise ratios for *SS* phases. 1-TANN is the original transversal (T) component obtained after rotation. The deconvolution window of 85 s is marked on the trace. The *SS* arrival peak is displayed in red. 2-TANN is the inverse filter for deconvolution generated by the *SS* waveform within the time window marked on the original (1-TANN) trace. 3-TANN displays the trace after deconvolution. To enhance the signal of coherent phases summation of all T traces is performed.

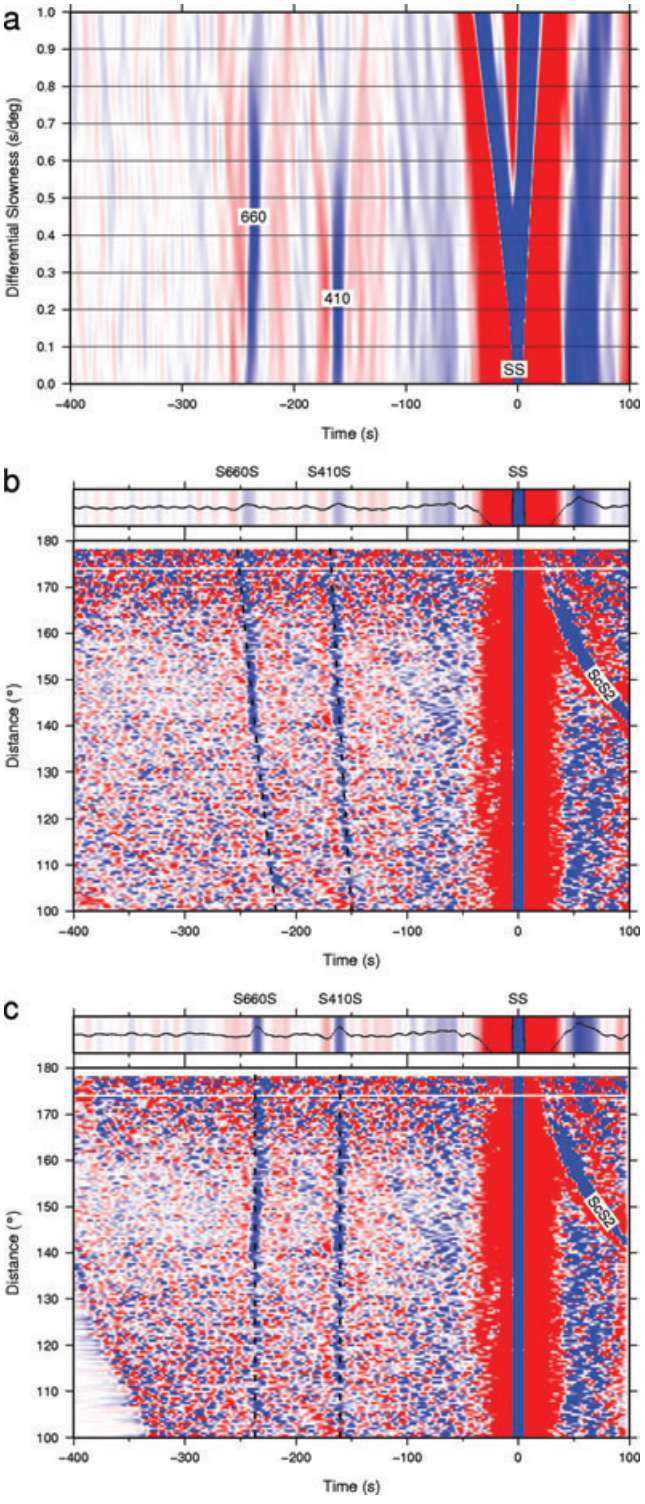

Figure 6. (a) Slant stack of *SS* data with a reference distance of 140°. The discontinuity phases should be picked at the corresponding differential slowness. (b) Binning stacks of all *SS* precursor data from the entire transect shown in Fig. 2. All traces are aligned by the *SS* arrivals and stacked in distance bins. On the top is the summation trace. (c) *SS* precursor data after moveout correction with a reference distance of 140°. Discontinuity phases are vertically aligned and can be well recognized in the summation trace on the top. For a, b and c, the positive amplitudes are in blue and the negative in red.

trace. After the moveout effect is corrected in Fig. 6(c), both phases appear parallel to the *SS* phase and can be clearly recognized in the summation trace.

Fig. 7(a) is a CMP stack profile for *SS* precursors along the entire transect. Bounce points within the green frame in Fig. 2(a) are considered. The area may be too big to enable a distinction between the different tectonic regions but shows, nevertheless, very coherent signals from the major upper-mantle discontinuities and some other interesting phases. The most significant features are the MTZ discontinuities, the 410 and the 660. Both phases are delayed by ∼4 s from 85°E to 140°E, which may be caused by a low *S*-wave velocity anomaly in the upper mantle. The 520 phase is weak and non-continuous. A negative phase below the 410 appears to be significant and can be observed nearly along the entire profile. The shallower part is however strongly disturbed by the big *SS* phase. In Fig. 7(b) we cut out the main *SS* waveform to −10 s and raised the *SS* sidelobe by a 100-s high-pass filter. Some shallow phases are recovered by this approach. The continental Moho can be seen from 70°E to 134°E with its deepest part located in Tibet at 90°E. East of 135°E, the Moho phases from the oceanic plate are too shallow to enable detection. A negative phase below the Moho can be followed from ∼50 s (∼120 km depth) in the west to ∼30 s (∼70 km depth) to east China at 134°E. The Lehmann discontinuity can be identified along the entire profile at ∼100 s (∼250 km depth).

To study the lateral variations of the different discontinuities we performed three parallel profiles from north to south where the most bounce points are located (see Fig. 2b). Detailed lateral variations of the crust and mantle discontinuities can be determined by looking at the different profiles of *SS* precursor data by CMP stacking method. The three profiles are represented by 35 boxes with size of 10° along latitude and 4° along longitude and a lateral overlapping of 1° (Fig. 8). Within each box *SS* waveforms are stacked according to the distribution of bounce points. A 12-s three-pole low-pass filter is applied to the stacks to increase the phase correlation. From west (75°E) to east (180°E) the profile covers a longitude range of ∼100° and passes through different tectonic settings, as described in the previous sections. The Tibetan region lies between boxes 2 and 10. The NC is located between boxes 11 and 19. The Sea of Japan and the Kuril subduction zone are located between boxes 20 and 25. Kamchatka and the Pacific plate along with the Bering Sea form part of the easternmost boxes from 26 to 35.

As seen from the whole data stacks (Fig. 6) the Moho reflection is masked by the strong *SS* phase. By carefully inspecting the *SS* stacks in different boxes we identified the Moho reflection signals clearly shown on the three profiles from Fig. 8. In Fig. 9 the procedure used to get the clear Moho phases hidden behind the waveforms is explained in more detail. Fig. 9(a) shows some sample stacks for boxes 5, 19 and 31, located in Tibet, east China and NW Pacific. The boxes are chosen to represent different tectonic settings from the ocean, a part of stable continent and the high-elevated plateau, with the Moho depth variations from less than 20 km to ∼80 km. The corresponding *SS* precursors may arrive at times of 10–35 s. It appears difficult to identify the Moho reflections as they are close to or inside the *SS* sidelobes. Theoretically, the deconvolved *SS* spikes should appear as nearly symmetric pulses. However this is not the case for the stacks of boxes 05 and 19. As a reference we swapped the *SS* waveform on the positive time axis around zero and overlain them on the negative time axis. While stack 31 is more or less symmetric, stacks 05 and 19 have significant contribution from the Moho reflections. Thus, by looking at *SS* waveform symmetry it is possible to detect shallow reflectors like the Moho at different depths. The Moho reflection is more clear when the Moho is deep

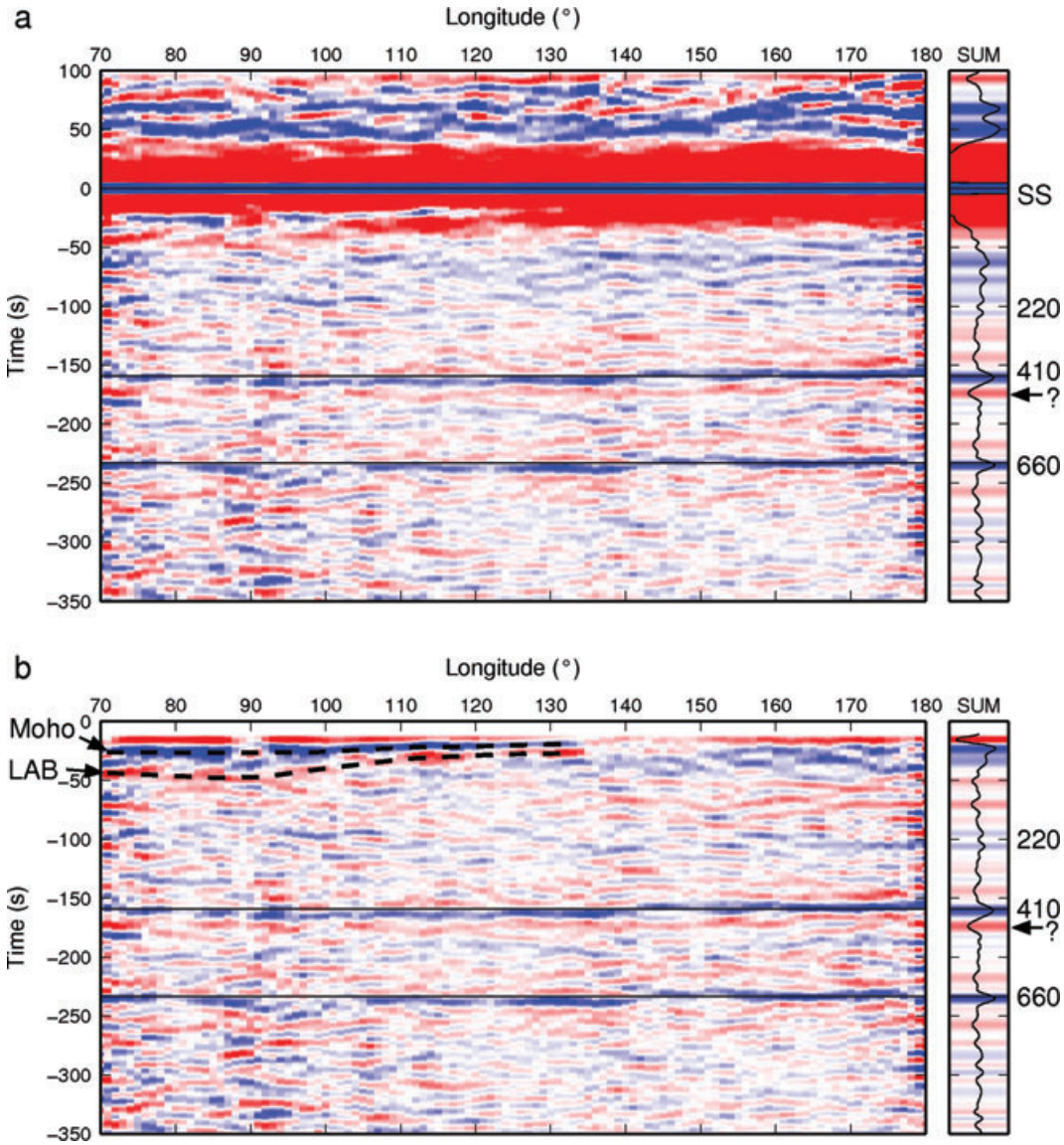

Figure 7. (a) CMP stack profile for *SS* precursors along the entire transect. Bounce points within the green frame in Fig. 2(a) are considered. Moveout-corrected individual *SS* waveform data are stacked in bins of 4° of bounce point longitude with a step of 1°. Positive amplitudes are coded in blue, negative in red. (b) Same section as (a) but after removing the big *SS* waveform to −10 s and applying a 100-s high-pass filter. Shallow phases have been recovered by this approach, so that at the end we are able to observe the continental Moho and LAB, the Lehmann discontinuity in addition to the 410 and the 660.

(e.g. Tibet) and becomes invisible when the Moho is too shallow, as in the case of an oceanic crust (Fig. 9a). Waveform modelling may provide useful information about the Moho depths (Rychert & Shearer 2010). Here we try to separate the Moho phase from the *SS* waveforms. After deconvolution and 12-s low pass, we cut out the large *SS* spike at time of the first negative peak (∼10s before the *SS* arrival) and apply a 100-s high-pass filter to restore the downwelling branch of the traces. By doing so we cut or remove all information from depths shallower than 20 km, but get clear Moho signals for larger depths. The results are shown in Fig. 9(b). The Moho phase is clearly visible for boxes 05 and 19 but is too shallow to be resolved in box 31.

5 OBSERVATIONS

The image presented in Fig. 7 has a lot of information from the different discontinuities but unfortunately is including bounce points from very distant regions stacked together in a single trace. To reduce this effect and have a more accurate definition of the discontinuities described in every summation trace we decided to perform our interpretation of the *SS* precursors data based on the central profile from Fig. 8. This profile has the most bounce points and runs along a series of tectonically very interesting regions and has very clear upper-mantle phases along with Moho and LAB discontinuities.

The resulted section is shown in Fig. 10. Waveforms of *SS* precursor data are superimposed on a recent seismic tomography by Kustowski *et al.* (2008). The summation trace is plotted on the right-hand side where it is possible to recognize at least three prominent positive phases (in blue) along the entire profile, also on the summation trace (marked Moho), 410 and 660, respectively. The first phase from top to bottom is located at depths less than 100 km between 75°E and 135°E. As explained above this is the Moho phase recovered from the *SS* sidelobes. The Moho depth varies along the

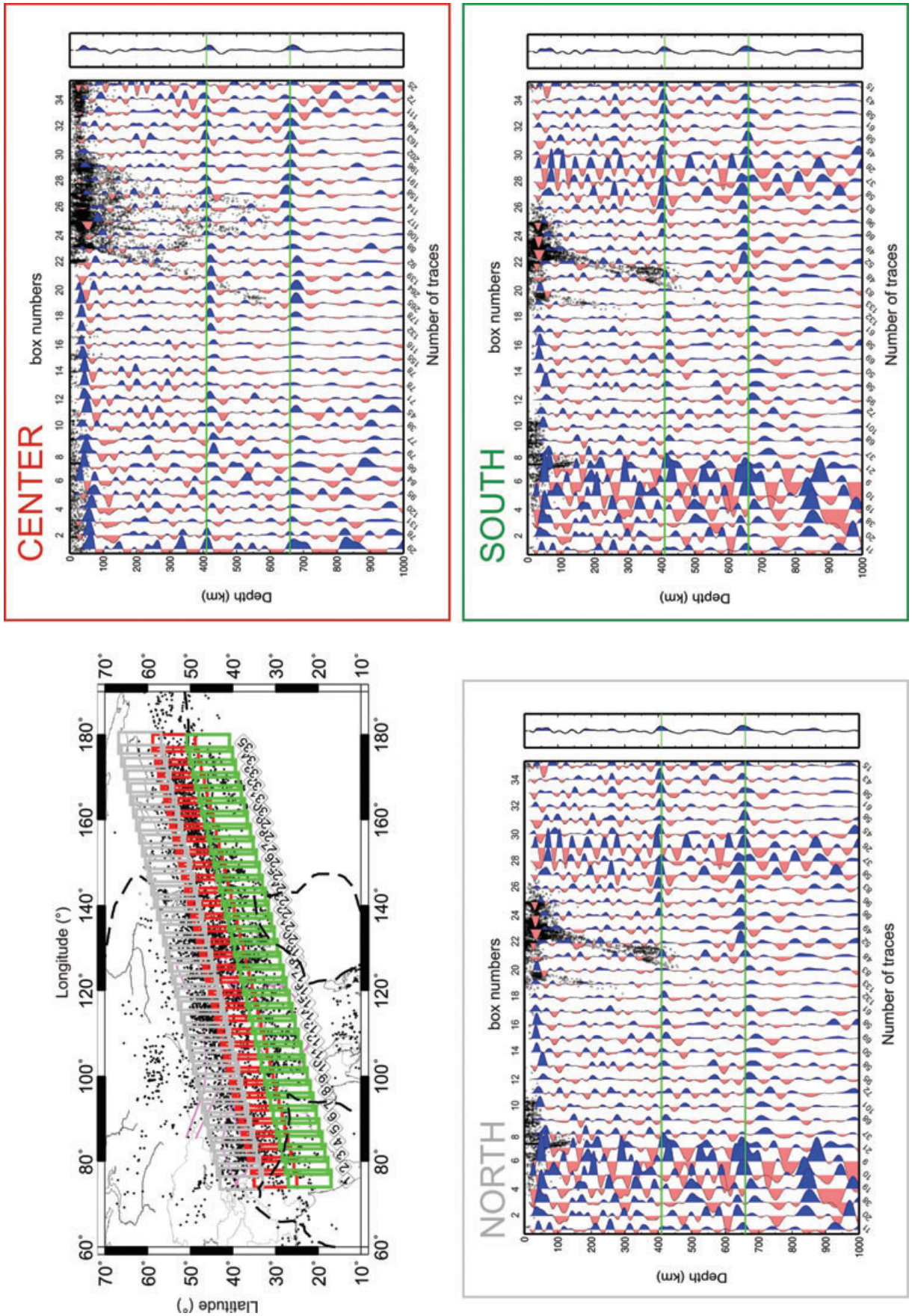

Figure 8. The map shows the north, centre and south profiles in which the study area was divided. The black dots on the map are the *SS* bounce points. Every profile has 35 boxes with 1° overlap and every box (size is 10° × 4°) is used to obtain the summation trace representative of each box. The labels numbered from 1 to 35 beneath the green boxes indicate the box numbers for all three profiles. The different profiles north (grey), centre (red) and south (green) obtained from the stacked traces are presented according to their box numbers. The number of traces can be seen at the bottom of every stacked trace. The black dots of the profile are earthquakes displayed to better visualize the subduction zones.

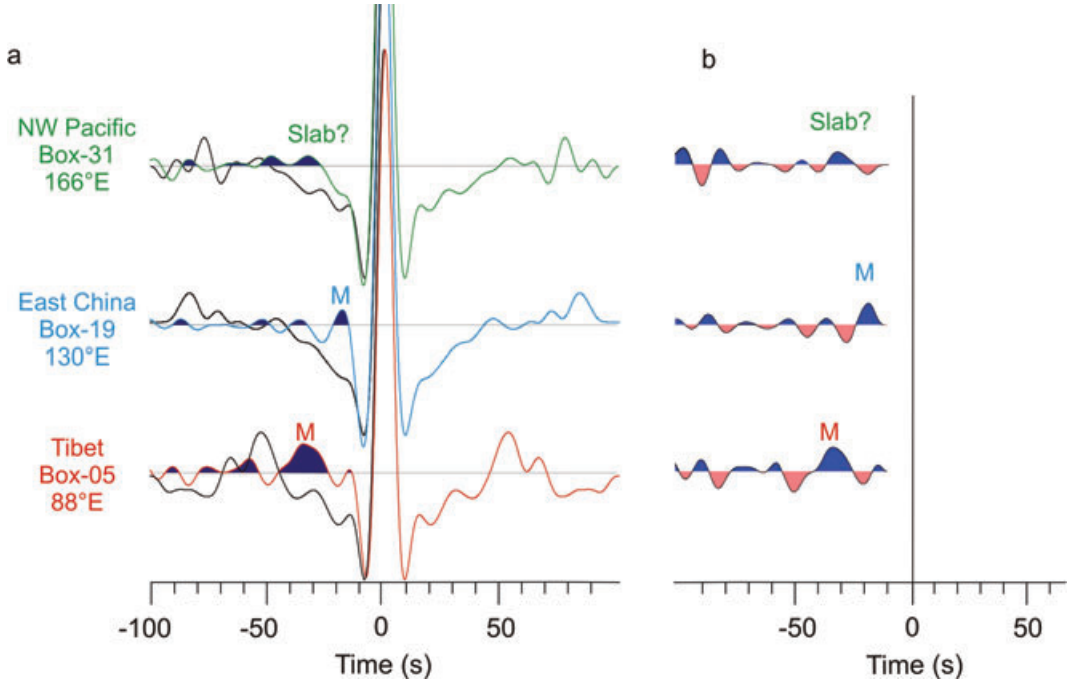

Figure 9. (a) Three summation traces chosen from different regions from the west (red trace) beneath Tibet, the centre of the profile (blue trace) beneath eastern China and from the NW Pacific ocean on the east (green trace). The Moho signal is separated from the sidelobe in every trace beneath the continent but is absent beneath the ocean. Waveforms on the positive time axis are mirrored around 0 s and plotted on the negative time axis (black lines). (b) Same traces after removal of the big *SS* spikes and a 100-s high-pass filter, identical to the traces plotted in Figs 8 and 10.

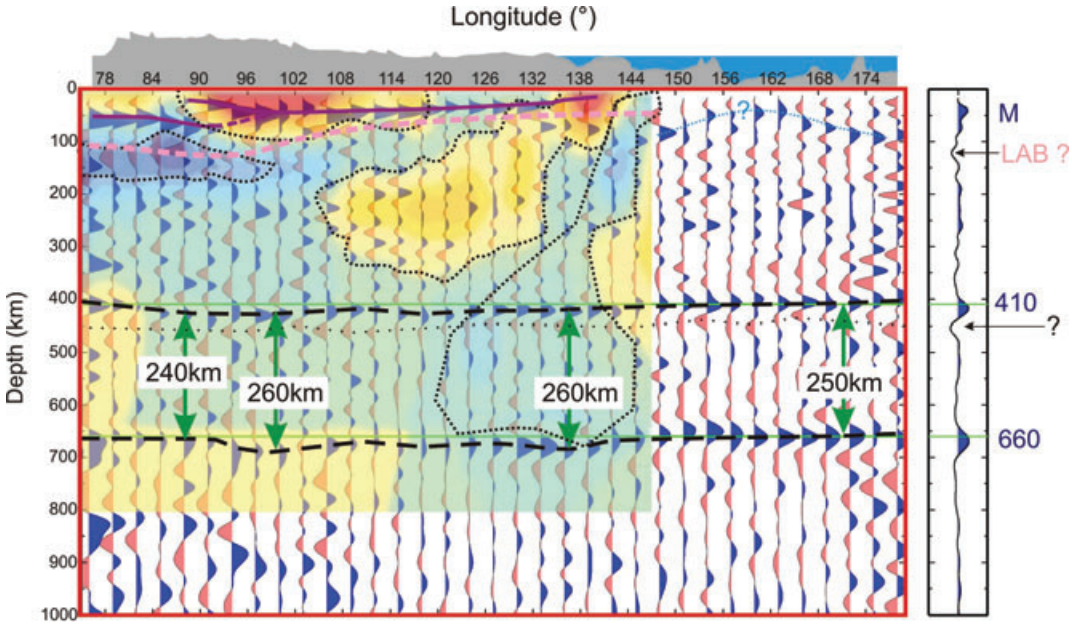

Figure 10. The stacked traces from the central profile are used for the interpretation. The violet line represents the phases interpreted here as the Moho (M). The M is *ca*. 80-km thick beneath Tibet and becomes progressively thinner towards the east until it is too shallow to be detected by this method beneath the ocean (east of 138°E). Beneath the Moho a negative phase interpreted here as the LAB (pink line) can be followed beneath the continental crust. On the east, phases from the Kuril and the Aleutian subduction zones (sky-blue dotted line) have their shallowest point beneath 162°E at the joint tip of both subducted plates. The 410 and 660 discontinuities (dashed black lines) highlight the topography of the MTZ in reference to the IASPEI arrivals times (green lines) for the 410 and 660, respectively. This section includes some features (marked as black dotted lines) from tomographic results (Kustowski *et al.* 2008) with high-velocity (sky-blue colour) and low-velocity (yellow-orange colour) anomalies along the entire profile. The MTZ present local variations in thickness and seems to be thinner on the west (240 km), intermediate on the east (250 km) and thick in the centre of the profile with (∼260 km). Beneath the 410 a low-velocity layer can be traced along the entire profile (dotted line) in accordance with observations from Vinnik *et al.* (2004). The summation trace on the right also shows the presence of the major upper-mantle discontinuities along with others as the Moho, the LAB and the 480(?).

profile with the deepest part located beneath Tibet on the western side. It reaches its maximum depth of 80 km at ∼90°E where it is possible to recognize a shallower phase at the same longitude but at 30 km depth. The Moho gradually shallows to a depth of 30–40 km in the stable continent (110°E–130°E) and becomes progressively less clear east of 135°E towards the position of the Pacific Ocean and the Kamchatka Peninsula.

The presence of a relatively clear negative phase (marked LAB on the summation trace) can be seen in Fig. 10 between 75°E and 105°E at a depth of approximately 120 km. It becomes shallower east of 105°E and seems to be accompanying the shape of the Moho phase. This negative phase is probably indicating the presence of the LAB being deeper on the west beneath Tibet and shallower towards the east beneath the oceanic plate.

At greater depths, it is possible to recognize two clear phases that are better seen on the easternmost part of the profile. The first is located at 410 km at 180°E and becomes a little deeper at 135°E where the subducted plate is supposed to be present. The second phase is located at 660 km and accompanies the first one in shape, that is, it becomes deeper at the same position. Both phases are related to the 410 and 660 discontinuities and seem to be less clear west of 135°E where they appear to be a little deeper that the expected times. The 520 can be occasionally observed mostly on the eastern part of the profile. Below the 660 there are not many coherent signals showing presence of other discontinuities in the lower mantle.

6 DISCUSSIONS AND CONCLUSION

For a better understanding of the interpreted data we separate the observations according to the major phases in the lithosphere and the mantle detected in this study. They are the Moho, the LAB and the 410 and the 660 mantle discontinuities (Fig. 10).

6.1 The Moho

We explore information about crustal thicknesses along our profile contained in the *SS* precursor data. The images presented here show clear Moho signals where the Asian continent is located and very weak or no signal for those areas with very thin oceanic crust on the east of the study area. The deepest Moho signal is observed beneath the central Tibetan plateau at 90°E where it reaches a depth of 80 km. In this area the presence of intracrustal structures as detected by other authors (e.g. Wittlinger *et al*. 1998) suggest a very complex tectonic arrangement due to the interaction between the Indian and Asian lithospheres. Wittlinger *et al.* (1998) have also suggested that part of the velocity variations at depths of 50 km in this area might be related to crustal underthrusting of the TB beneath the QB giving the Altai Tagh Fault the character of an oblique plate boundary. This statement supports our observations as we also interpret the intracrustal phases, seen as double phases between 86°E–92°E as part of underthrusted crustal material. This becomes more evident at 92°E where the Moho has a very shallow phase at ∼40 and a deeper one at ∼80 km. Towards the east the Moho becomes progressively shallower until it is too thin to be detected by this method at the coast of China (i.e. 134°E).

In any case we must keep in mind that the resolution of the *SS* precursors might be influenced by the anomalies surrounding the *SS* bounce points at different depths implying that these measurements can only be regarded as a control for the Moho. Further studies will be needed to improve the quality of this method and to avoid biases related to wrong estimations in considering the right velocity model for every particular case. Shearer (1991) has also suggested that the measurements using *SS* precursors might have a resolution of that of the Fresnel zone, this means 15° around the specific bounce point. Another possibility for an induced wrong lecture of the Moho phases might be related to the detectability of the intracrustal phases at depth. For example, in the case of Tibet, many studies have shown the presence of strong conversions in the lower crust (e.g. Kind *et al.* 2002 called them crustal doublets) at 60 km beneath the area where we see the jump in Moho depths at 90°E. Other authors (e.g. Hirn *et al.* 1984) suggested an eastward movement of the Tibetan lithosphere after detecting different Moho depths along a seismic profile. They interpreted these variations as related to the presence of different intracrustal slices interacting due to the continental collision that lifted up the plateau and thickened the crust. Detecting the right conversion phase for the Moho must therefore be performed by integrating different geophysical studies. Li *et al.* (2000) have detected by receiver functions a phase that correlates well with our Moho (Fig. 11) at the same depth along our profile (between 115°E and 140°E). Recently, Nabelek *et al.* (2009) published receiver function data from a north–south transect at 85°E where it is possible to see a the good correlation between their results and our Moho topography along the same region (Fig. 12).

In a recent paper (Rychert & Shearer 2010) the authors have been able to map Moho depth variations in Asia as they recognized the differences between stacks from continental and ocean waveforms using *SS* precursors. This work shows similar results as those obtained by them for the Moho depths beneath Tibet (*ca*. 55–60 km at 30°N; 100°E) and also beneath north Korea in the western part of the Japan Sea (*ca*. 35 km at 40°N; 125°E).

On the easternmost part of the profile of Fig. 10 we are able to recognize some positive phases at depths between 50 and 100 km. These phases appear in regions where both subduction zones, the Aleutian on the east and Kuril on west are located. We suggest that these phases might be related to the subducted slabs as the shallowest phase depth coincides approximately with the convergence point of both subduction zones between boxes 30 and 31. The absence of similar structures in the profiles to the north and the south is indicating the local character of these phases, which might be related to the lack of seismicity at these depths for the subducted plates (see Fig. 8).

6.2 The LAB

The negative phases interpreted here as the LAB are clearly seen on the summation trace of Fig. 10. The best traces for the LAB are located beneath the Moho on the western part of the profile beneath the Tibetan plateau at a depth of ∼120 km and become weaker and shallower beneath east China. The LAB depth variation is consistent with surface wave tomographies (Huang *et al.* 2003; Priestley & McKenzie 2006) and receiver function studies (Kumar *et al.* 2006; Sodoudi *et al.* 2006; Chen *et al.* 2006, 2008), which generally agree that the lithosphere is thick in Tibet and west China and thins to less than 70 km beneath east China. The step in the Moho described before (see Moho discussion above) is accompanied by a jump in the depth of the LAB from 120 km west of 94°E to less than 100 km depth east of 100°E. The strongest and deepest LAB beneath Tibet is also consistent with the high-velocity lid shown in the background tomography (Kustowski *et al.* 2008) as they detected a high-velocity structure possibly related to the Indian lithosphere underthrusting the Asian lithosphere around 90°E. The depth difference between our methods could be a matter of different resolution and sampling

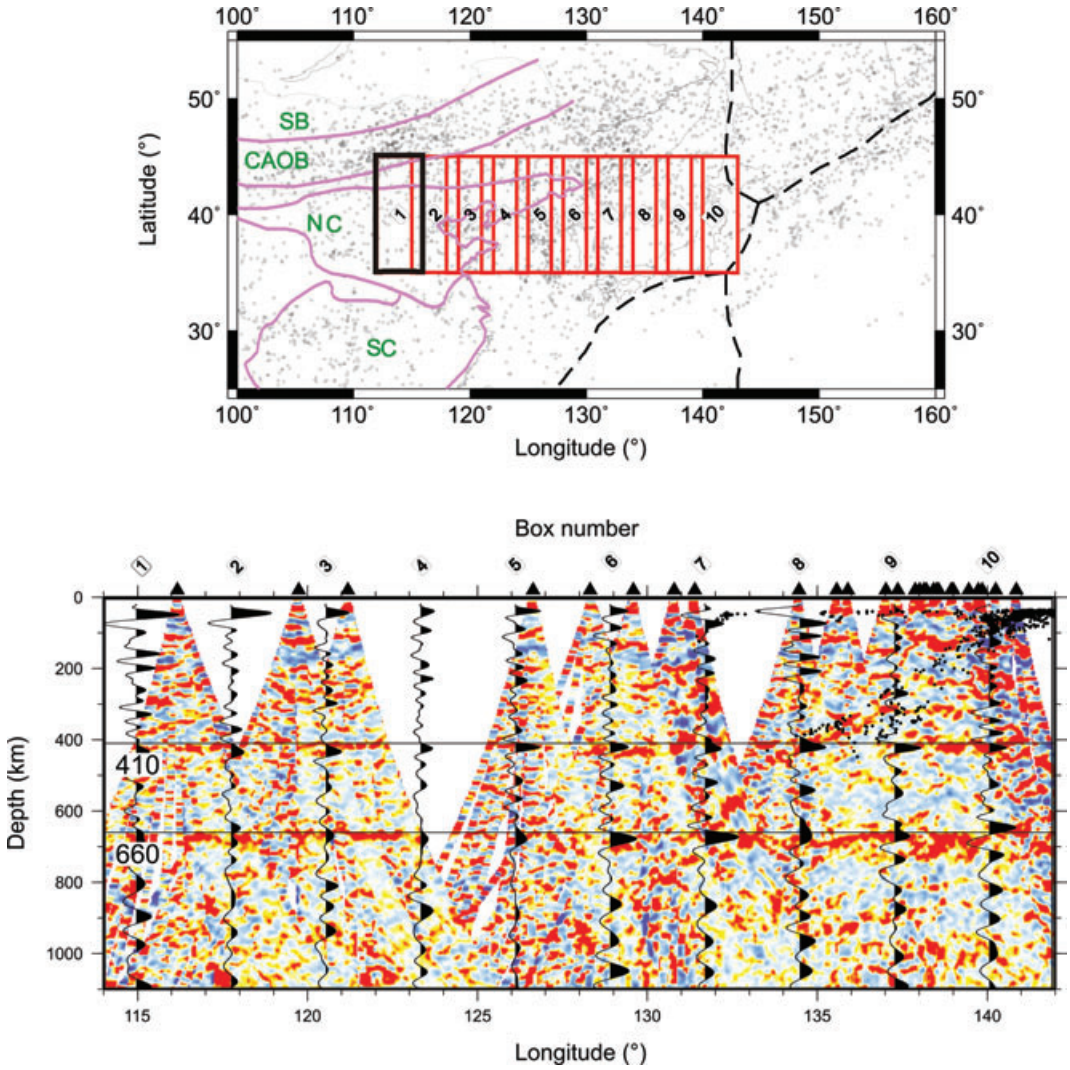

Figure 11. The map shows the position of the boxes for *SS* precursor performed to compare our data with previous PRF results from eastern Asia (Li *et al.* 2000). The boxes are 10° × 5° in size with an overlapping of 1° (see black box for size reference). In this figure, the authors have shown the positive phases in red colour and negative in blue colour as they investigated MTZ along a profile using broad-band data from different studies between 116°E and 141°E. We superimposed the stacked traces along the same profile with all positive phases from *SS* highlighted in black colour. It is possible to see that the Moho phases detected by our *SS* study in the upper 100 km correlate very well with the first phases detected by the PRF's revealing a good agreement for the different crustal depths along the profile. There is also a good correlation between both methods for the MTZ zone discontinuities as they are both shifted downwards at the position of the slab between 120° and 144°E and start to become shallower west of 120°E.

regions. For Priestley & McKenzie (2006) the LAB seems to be deeper than in our observations—*ca*. 250 km beneath Tibet compared to the 120 km that we observe in our data—but this could be related to local variations at depth in slightly different regions with different resolution and methodologies. However, the overall variation of the LAB seems to be consistent in both studies, that is, deeper beneath Tibet and shallower towards the north where the NC is located (60 km in our study and 100 km for Priestley & McKenzie 2006). This situation is interesting and reflects the importance of further studies to constrain and better determine the depth of the LAB in this region.

6.3 The Lehmann discontinuity

It has been suggested that the Lehmann discontinuity has a regional distribution and is more often observed beneath continents (e.g. Gu *et al.* 2001). Although our profiles sample much of the Eurasian continent and part of the oceanic upper mantle it is not clear if some phases at 220 km depth are related to the presence of this discontinuity. This situation could be related with the presence of a low-velocity anomaly detected by tomography (Kustowski *et al.* 2008) on the west of the subducted slab at this depth. East of the subduction zone and beneath the oceanic crust there are no clear phases that could be indicating the presence of the Lehmann discontinuity. This is in agreement with previous studies (e.g. Gossler & Kind 1996; Gu *et al.* 1998; Flanagan & Shearer 1998) that failed to detect this phase. In Fig. 8, relatively coherent phases between boxes 26 and 35 for the north and south profiles might be indicating the presence of the Lehmann discontinuity at *ca*. 260 km depth. Although the absence of these phases at the central profile where the number of traces for the same boxes is clearly higher might be suggesting that the aspect of the discontinuity is disturbed by the velocity anomaly described before. The strongest indication for

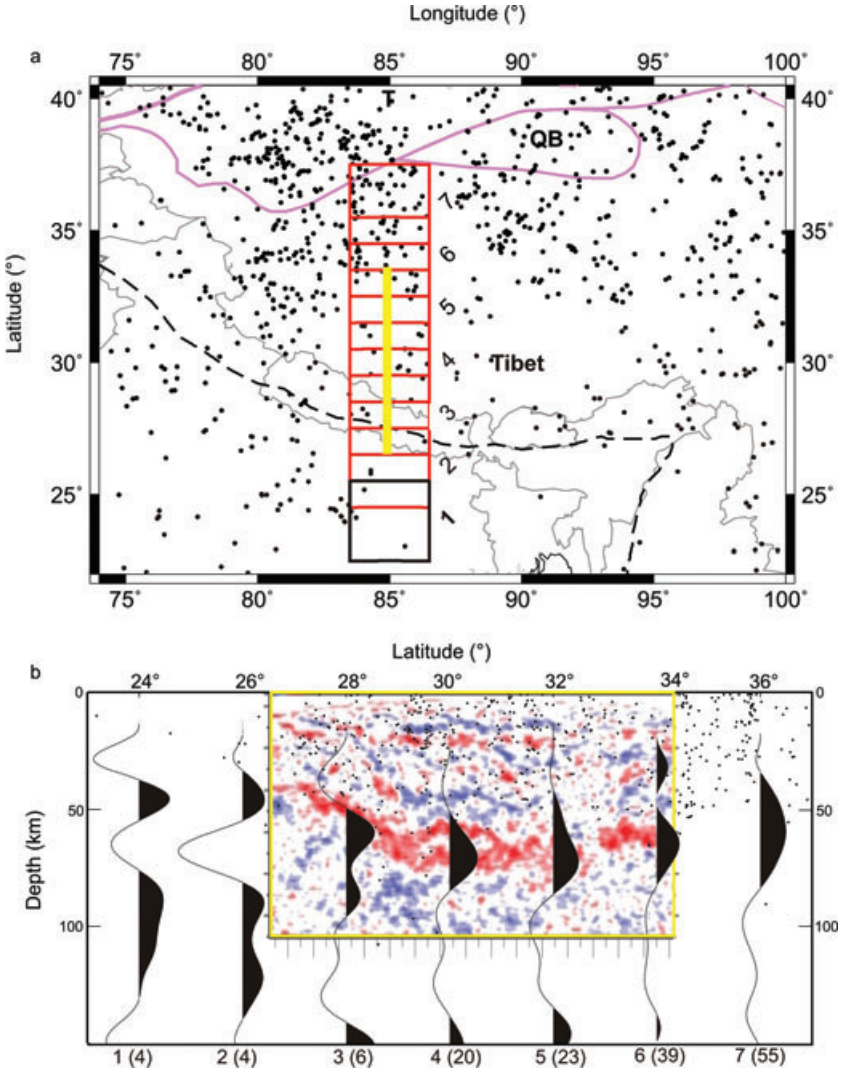

Figure 12. (a) Map showing the position of the boxes preformed to compare *SS* with PRF results from the Hi-Climb project (yellow line). The boxes are 5° × 5° with 2° overlapping (see black box as reference). The PRF results (Nabelek *et al.* 2009) that are located along a N–S profile at 85°E show a double phase for the Moho at 60 and 75 km. We performed a similar profile to verify our Moho measurements using *SS* precursor. At this scale we are not able to detect this double Moho phase but we see a clear overall correlation for the Moho depths in both independent studies between 27°N and 34°N.

the presence of this phase can be seen in Fig. 7 where all the data are integrated. This is suggesting that the Lehmann discontinuity can only be clearly seen by integrating huge amounts of data as in the case of Fig. 7, however we need to keep in mind that the big area described in this figure will make it almost impossible to determine if there are some correlations between the crustal blocks and the different lithospheric units observed along this corridor.

6.4 Thickness of the MTZ

The MTZ may become thinner in hot and thicker in cold regions (e.g. Bina & Helffrich 1994). In our profile of Fig. 10 we do not find any evidence of a strongly thinned or thickened MTZ. The topography of the 410 and the 660 discontinuities is shifted downwards in an effect that is probably induced by the presence of a low-velocity zone (e.g. Kustowski *et al.* 2008) above the subducted slab between 105°E and 140°E. The 410 does not appear to be shifted upwards due to the presence of slab as suggested by other authors (e.g. Tonegawa *et al.* 2005) where they detected an uplift of 30 km for the 410 with high-resolution images from receiver functions. This suggests that the cold slab is only able to shift the 410 upwards within a very local region that is far from being resolved by the method used in this work.

The depression of both the 410 and the 660 in this area coincides with the place along the profile with the thickest MTZ *ca*. 260 km. Towards the east, beneath the ocean the thickness is normal at 250 km and towards the west beneath the Asian continent the MTZ is thinnest beneath Tibet (*ca*. 240 km). The depression of the 660 beneath the Sea of Japan is probably suggesting that cold material has been introduced to the MTZ due to the presence of the slab. The stagnation of the slab (Fukao *et al.* 1992) is interpreted as being responsible for the anomalous distribution of cold oceanic material inside the MTZ that pushes the 660 downwards (e.g. Li & Yuan 2003). As the subduction proceeds towards the west a part of the flattened slab, as observed in tomographic images, is probably adding some extra weight to the 660 km depth discontinuity.

Therefore, it is possible to conclude that the *SS* precursors are an important tool that could help us to understand and determine the characteristics of some of the major discontinuities in the upper

mantle and the lithosphere. The variability of the composition and temperature induced by the presence of a subducting slab as in our profile leaves much place for speculation concerning the distribution and clearness of the phases at one or the other side of the subduction zone. Therefore the best suited regions for the identification of both the 410 and the 660 seems to be located beneath the oceans whereas for the depth of the LAB and the Moho they seem to be more easily detected beneath the continents. This effect is definitely related to the presence of the subducting plate that, as a cold, wet body, modifies the geodynamics of the asthenosphere, and therefore the distribution of the upper-mantle anomalies. It is important to remember that the number of traces used to obtain the summation traces is higher beneath the eastern part the study area. Whether this is just coincidental or not can only be proved with more data.

On the summation trace for all the data (Fig. 10) it is possible to recognize a negative phase right underneath the 410 (at a depth of *ca*. 450 km) that can be traced almost along the entire profile from west to east. A similar negative phase at a depth of 480 km was described by Vinnik *et al.* (2004) beneath the Afro-Arabian hotspot by using *S* receiver functions. They interpreted it as being related to the origin of another mantle plume trapped in the MTZ. In our data we find new evidence supporting the presence of a low-velocity layer at nearly the same depth but as it is observed almost along the entire profile it might suggest that this layer has a more regional distribution. In any case, more data will be needed to shed light on this subject. A similar signal was found with *ScS* reverberations under east China (Revenaugh & Sipkin 1994) and east of Japan (Bagley *et al.* 2009) but atop the 410.

ACKNOWLEDGMENTS

The work is funded by the Deutsche Forschungsgemeinschaft. Waveform data were obtained from the GEOFON, the SZGRF and IRIS data centres. Seismic Handler software package (Stammler 1993) is used for data processing. Most figures are plotted using Generic Mapping Tools (Wessel & Smith 1998). We thank two anonymous reviewers for their comments and suggestions as they helped us to improve the quality of the manuscript.

REFERENCES

Anderson, D.L., 1995. Lithosphere, asthenosphere, and perisphere, *Rev. Geophys.,* **33,** 125–149.

Bagley, B., Courtier, A.M. & Revenaugh, J., 2009. Melting in the deep upper mantle oceanward of the Honshu slab, *Phys. Earth planet. Inter.,* **175**(3–4), 137–144, doi:10.1016/j.pepi.2009.03.007.

Barrell, J., 1914. The strength of the Earth's crust, *J. Geol.,* **22,** 655–683.

Bijwaard, H., Spakman, W. & Engdahl, E.R., 1998. Closing the gap between regional and global travel time tomography, *J. geophys. Res.,* **103**(B12), 30 055–30 078.

Bina, C.R. & Helffrich, G., 1994. Phase transition Clapeyron slopes and transition zone seismic discontinuity topography, *J. geophys. Res.,* **99,** 15853–15860.

Chambers K, Deuss A. & Woodhouse, J.H., 2005a. Reflectivity of the 410-km discontinuity from PP and SS precursors, *J. geophys. Res.,* **110**(B2), B02301, doi:10.1029/2004JB003345.

Chambers, K., Woodhouse, J.H. & Deuss, A., 2005b. Topography of the 410-km discontinuity from PP and SS precursors, *Earth planet. Sci. Lett.,* **235**(3–4), 610–622.

Chen, L., Zheng, T.Y. & Xu, W.W., 2006. A thinned lithospheric image of the Tanlu fault zone, eastern China: constructed from wave equation based receiver function migration, *J. geophys. Res.,* **111,** B09312, doi:10.1029/2005JB003974.

Chen, L., Tao, W., Zhao, L. & Zheng, T.Y., 2008. Distinct lateral variation of lithospheric thickness in the northeastern North China Craton, *Earth planet. Sci. Lett.,* **267,** 56–68.

Deuss, A., 2009. Global observations of mantle discontinuities using SS and PP precursors, *Surv. Geophys.,* **30**(4–5), 301–326.

Deuss, A. & Woodhouse, J.H., 2001. Seismic observations of splitting of the mid-transition zone discontinuity in Earth's mantle, *Science,* **294,** 354–357.

Deuss, A. & Woodhouse, J.H., 2002. A systematic search for upper mantle discontinuities using SS-precursors, *Geophys. Res. Lett.,* **29,** 901–904.

Dueker, K. & Sheehan A., 1997. Mantle discontinuity structure from mid-point stacks of converted P to S waves across the Yellowstone hotspot track, *J. geophys. Res.,* **102**(B4), 8313–8327.

Eaton, D.W., Darbyshire, F., Evans, R.L., Grütter, H., Jones, A.G. & Yuan, X.H., 2009. The elusive lithosphere-asthenosphere boundary (LAB) beneath cratons, *Lithos,* **109,** 1–22.

Flanagan, M.P. & Shearer, P.M., 1998. Global mapping of topography on transition zone velocity discontinuities by stacking SS precursors, *J. geophys. Res.,* **103,** 2673–2692.

Frost, D.J., 2008. The upper mantle and transition zone, *Elements,* **4,** 171–176.

Fukao, Y., Obayashi, M., Inoue, H. & Nenbai M., 1992. Subducting slabs stagnant in the mantle transition zone, *J. geophys. Res.,* **97,** 4809–4822.

Gossler, J & Kind, R., 1996. Seismic evidence for very deep roots of continents, *Earth planet. Sci. Lett.,* **138,** 1–13.

Gu, Y.J. & Dziewonski, A.M., 2002. Global variability of transition zone thickness, *J. geophys. Res.,* **107,** 2135, doi:10.1029/2001JB000489.

Gu, Y., Dziewonski, A.M., & Agee, C.B., 1998. Global de-correlation of the topography of transition zone discontinuities, *Earth planet. Sci. Lett.,* **157,** 57–67.

Gu Y, Dziewonski, A.M. & Ekström G., 2001. Preferential detection of the Lehmann discontinuity beneath continents, *Geophys. Res. Lett.,* **28**(24), 4655–4558.

Helffrich, G., 2000. Topography of the transition zone seismic discontinuities, *Rev. Geophys.,* **38**(1), 141–158.

Hirn, A. *et al*., 1984. Crustal structure and variability of the Himalayan border of Tibet. *Nature,* **307,** 23–25, doi:10.1038/307023a0.

Huang, J. & Zhao, D., 2006. High-resolution mantle tomography of China and surrounding regions, *J. geophys. Res.,* **111,** B09305, doi:10.1029/2005JB004066.

Huang, Z., Su, W., Peng, Y., Zheng, Y. & Li, H., 2003. Rayleigh wave tomography of China and adjacent regions, *J. geophys. Res.,* **108,** 2073, doi:10.1029/2001JB001696.

Katsura, T. & Ito, E., 1989. The system Mg2SiO4-Fe2SiO4 at high pressures and temperatures: precise determination of stabilities of olivine, modified spinel and spinel, *J. geophys. Res.,* **94,** 15 663–15 670.

Kind, R., 1978. The reflectivity method for a buried source, *J. Geophys.,* **44,** 603–612.

Kind, R. *et al*., 2002. Seismic images of crust and upper mantle beneath Tibet: evidence for Eurasian plate subduction, *Science,* **298**(5596), 1219–1221.

Kröner, A. *et al*., 2007. Accretionary growth and crust-formation in the central Asian Orogenic belt and comparison with the Arabian-Nubian shield, in *The 4-D Framework of the Continental Crust: Integrating Crustal Processes Through Time,* pp. 181–209, eds Hatcher, R.D., Carlson, M.P., McBride, J.H. & Catalan, J.M., Geological Society of America.

Kröner, A., Hegner, E., Lehmann, B., Heinhorst, J., Wingate, M.T.D., Liu, D.Y. & Ermelov, P., 2008. Palaeozoic arc magmatism in the central Asian Orogenic belt of Kazakhstan: SHRIMP zircon ages and whole-rock Nd isotopic systematics, *J. Asian Earth Sci.,* **32**(2–4), 118–130.

Kumar, P., Yuan, X., Kind, R. & Ni, J., 2006. Imaging the colliding Indian and Asian lithospheric plates beneath Tibet, *J. geophys. Res.,* **111,** B06308, doi:10.1029/2005JB003930.

Kusky, T.M., Windley, B.F. & Zhai, M.G., 2007. Tectonic evolution of the north China block: from Orogen to Craton to Orogen, in *Mesozoic Sub-Continental Lithospheric Thinning Under Eastern Asia,* pp. 1–34,

Vol. 280, eds Zhai, M.G., Windley, B.F., Kusky, T.M. & Meng, Q.R., Geological Society of London, Special Publication, Bath.

Kustowski, B., Ekström, G. & Dziewonski, A.M., 2008. The shear-wave velocity structure in the upper mantle beneath Eurasia, *Geophys. J. Int.,* **174,** 978–992.

Li, X. & Yuan, X., 2003. Receiver functions in northeast China: implications for slab penetration into the lower mantle in northwest Pacific subduction zone. *Earth planet. Sci. Lett.,* **216**(4), 679–691.

Li, X., Sobolev, S., Kind, R., Yuan, X. & Estabrook, C., 2000. A detailed receiver function image of the upper mantle discontinuities in the Japan subduction zone, *Earth planet. Sci. Lett.,* **183,** 527–541.

Li, X., Kind, R., Yuan, X., Sobolev, S.V., Hanka, W., Ramesh, D.S., Gu, Y.G. & Dziewonski, A.M., 2003. Seismic observation of narrow plumes in the oceanic upper mantle, *Geophys. Res. Lett.,* **30,** 1334, doi:10.1029/2002GL015411.

Nabelek, J. *et al*. (the Hi-CLIMB Team), 2009. Underplating in the Himalaya-Tibet collision zone revealed by the Hi-CLIMB experiment, *Science,* **352,** 1371–1374.

Neele, F., De Regt, H. & VanDecar J., 1997. Gross errors in upper-mantle discontinuity topography from underside reflection data, *Geophys. J. Int.,* **129,** 194–204.

Petersen, N., Vinnik, L., Kosarev, G., Kind, R., Oreshin, S. & Stammler, K., 1993. Sharpness of the mantle discontinuities, *Geophys. Res. Lett.,* **20,** 859–862.

Priestley, K. & McKenzie, D., 2006. The thermal structure of the lithosphere from shear wave velocities, *Earth planet. Sci. Lett.,* **244,** 285–301.

Revenaugh, J. & Sipkin, S.A., 1994. Seismic evidence for silicate atop the 410-km mantle discontinuity, *Nature,***369,** 474–476.

Ringwood, A.E., 1969. Phase transformations in the mantle, *Earth planet. Sci. Lett.,* **5,** 401–412.

Rychert C.A. & Shearer P., 2010. Resolving crustal thickness using SS waveform stacks, *Geophys. J. Int.,* **180,** 1128–1137, doi:10.1111/j.1365-246X.2009.04497.x.

Shearer, P.M., 1990. Seismic imaging of upper-mantle structure with new evidence for a 520-km discontinuity, *Nature,* **344,** 121–126.

Shearer, P.M., 1991. Constraints on upper-mantle discontinuities from observations of long-period reflected and converted phases, *J. geophys. Res.,* **96,** 18 147–18 182.

Shearer, P.M., 1993. Global mapping of upper mantle reflectors from long-period SS precursors, *Geophys. J. Int.,* **115,** 878–904.

Shearer, P.M., 1996. Transition zone velocity gradients and the 520-km discontinuity, *J. geophys. Res.,* **101,** 3053–3066.

Shearer, P.M., 2000. Upper mantle seismic discontinuities, in *Earth's Deep Interior: Mineral Physics and Tomography from the Atomic to the Global Scale,* pp. 115–131, Vol. 117, AGU Geophysical Monograph.

Shearer, P.M. & Masters, T.G, 1992. Global mapping of topography on the 660 km discontinuity, *Nature,* **355,** 791–796.

Shearer, P.M., Flanagan M.P. & Hedlin, M.A.H., 1999. Experiments in migration processing of SS precursor data to image upper mantle discontinuity structure, *J. geophys. Res.,* **104,** 7229–7242.

Sodoudi, F., Yuan, X., Liu, Q., Kind, R. & Chen, J., 2006. Lithospheric thickness beneath the Dabie Shan, central eastern China from S receiver functions, *Geophys. J. Int.,* **166**(3), 1363–1367.

Stammler, K., 1993. SeismicHandler: programmable multichannel data handler for interactive and automatic processing of seismological analysis, *Comput. Geosci.,* **19,** 135–140.

Tonegawa T., Hirahara K. & Shibutani T., 2005. Detailed structure of the upper mantle discontinuities around the Japan subduction zone imaged by receiver function analyses, *Earth Planets Space,* **57,** 5–14.

Vacher, P., Mocquet, A. & Sotin, C., 1998. Computation of seismic profiles from mineral physics: the importance of the non-olivine components for explaining the 660 km depth discontinuity, *Phys. Earth planet. Inter.,* **106,** 275–298.

Van Der Hilst, R.D., Engdahl, E.R., Spakman, W. & Nolet, G., 1991. Tomographic imaging of subducted lithosphere below northwest Pacific island arcs, *Nature,* **353,** 37–42.

Van Der Voo, R., Spakman, W. & Bijwaard, H., 1999. Mesozoic subducted slabs under Siberia, *Nature,* **397,** 246–249.

Vinnik, L., Kosarev, G. & Petersen, N., 1996. Mantle transition zone beneath Eurasia, *Geophys. Res. Lett.,* **23,** 1485–1488.

Vinnik, L.P.; Farra, V. & Kind, R., 2004. Deep structure of the Afro-Arabian hotspot by S receiver functions, *Geophys. Res. Lett.,* **31,** L11608, doi:10.1029/2004GL019574.

Wessel, P. & Smith, W.H.F., 1998. New, improved version of the Generic Mapping Tool released, *EOS, Trans. Am. geophys. Un.,* **79,** 579.

Windley, B.F., Alexeiev, D., Xiao, W.J., Kroner, A. & Badarch, G., 2007. Tectonic models for accretion of the central Asian Orogenic belt, *J. geol. Soc.,* **164,** 31–47.

Wittlinger, G., Tapponnier, P., Poupinet, G., Mei, J., Danian, S., Herquel, G. & Masson, F., 1998. Tomographic evidence for localized lithospheric shear along the Altyn Tagh fault, *Science,* **282**(5386), 74, doi:10.1126/science.282.5386.74.

Yuan, X., Ni, J., Kind, R., Sandvol, E. & Mechie, J., 1997. Lithospheric and upper mantle structure of southern Tibet from a seismological passive source experiment, *J. geophys. Res.,* **102**(B12), 27 491–27 500.

Zhao, D., 2004. Global tomographic images of mantle plumes and subducting slabs: insight into deep Earth dynamics, *Phys. Earth planet. Inter.,* **146,** 3–34.